

# Efficiencies of Coated and Perforated Semiconductor Neutron Detectors

J. Kenneth Shultis and Douglas S. McGregor, *Member, IEEE*

**Abstract**—Previous experimental results indicated that boron-filled perforations within a semiconductor diode detector increase the thermal neutron detection efficiency. In this paper, two basic perforation designs, circular holes and parallel trenches, are analyzed using a simple Monte Carlo model to estimate their potential as high-efficiency thermal neutron detectors. The modeling results indicate that thermal-neutron intrinsic detection efficiencies exceeding 25% can be realized for single coated devices, and efficiencies exceeding 50% can be realized for doubled or “sandwiched” devices.

**Index Terms**—Perforated detector, semiconductor neutron detector.

## I. INTRODUCTION

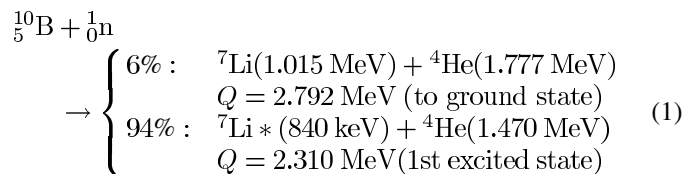
THIN-FILM coated semiconductor devices have been investigated for thermal neutron detection by a variety of research groups [1]–[14], all of which have generally used  $^{10}\text{B}$ ,  $^6\text{Li}$ ,  $^6\text{LiF}$ , and Gd coatings as the neutron reactive layer. Each of these listed neutron reactive materials has advantages and disadvantages. Although natural Gd has a very large thermal neutron cross section ( $\approx 47\,000$  barns) [15], its charged particle reaction products are of low energy, consisting mainly of conversion electrons whose primary emission energies do not exceed 250 keV. Charged particle reaction product energies from the  $^{10}\text{B}(n, \alpha)^7\text{Li}$  and the  $^6\text{Li}(n, t)^4\text{He}$  reactions range from 840 keV–2.73 MeV. Hence, because of these much larger emission energies compared to Gd reaction products, only  $^{10}\text{B}$  and the stable compound  $^6\text{LiF}$  are investigated in the present work.

The maximum thermal neutron detection efficiency for single-coated planar devices ranges from 4.0% to 4.6%, for  $^{10}\text{B}$  and the stable compound  $^6\text{LiF}$ , respectively, when using a lower level discriminator (LLD) setting of 300 keV [12]. The efficiency also depends upon the irradiation direction. A problem previously encountered, now solved, involved peeling and delamination of the coatings from thin-film stresses introduced by the evaporative deposition. Film adhesion to the device surfaces was dramatically improved by simply etching tiny holes into the diode barrier surface before applying the conversion layers [10]. Due to the increased probability that reaction products

enter the semiconductor, the thermal neutron detection efficiency also increased when the same holes were refilled with evaporated or fine powders of the converter material [10], [16]. This led to the realization of a 13% thermal neutron detection efficiency for compound semiconductor diode designs [11]. It becomes clear that a detailed study of the perforation shapes and sizes can lead to an optimized design for high-efficiency neutron detectors. In the present work, a Monte-Carlo method is used to study geometric effects on thermal neutron detection efficiency for circular hole and parallel trench perforations filled with neutron reactive materials.

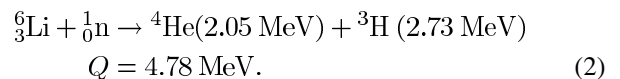
## II. BACKGROUND AND THEORETICAL CONSIDERATIONS

The  $^{10}\text{B}(n, \alpha)^7\text{Li}$  reaction leads to the following reaction products and branching ratios [17]:



The thermal neutrons absorbed by  $^{10}\text{B}$  produce energetic particles emitted at  $180^\circ$ . After absorption, 94% of the reactions leave the  $^7\text{Li}$  ion in its first excited state that rapidly de-excites to the ground state ( $\sim 10^{-13}$  seconds) by releasing a 480 keV gamma ray. The remaining 6% of the reactions result in the  $^7\text{Li}$  ion dropping directly to its ground state. The thermal neutron (0.0259 eV) microscopic absorption cross section is 3840 barns. The thermal cross section energy dependence is proportional to the inverse of the neutron velocity ( $1/v$ ) in much of the thermal energy range [15], [18]. Pure  $^{10}\text{B}$  has a macroscopic thermal neutron absorption cross section of  $500 \text{ cm}^{-1}$ .

The  $^6\text{Li}(n, t)^4\text{He}$  reaction leads to the following reaction products [17]:



Thermal neutrons absorbed by  $^6\text{Li}$  produce two energetic ions emitted in opposite directions. The thermal neutron microscopic absorption cross section is 940 barns. The neutron absorption cross section dependence is proportional to the inverse of the neutron velocity ( $1/v$ ) over much of the energy range [15], [18]. Li metal is a chemically reactive material typically unsuitable for thin film detectors, hence the compound  $^6\text{LiF}$  is often used,

Manuscript received April 21, 2005; revised December 19, 2005. This work was supported by the Defense Threat Reduction Agency under Contract 01-03-C-0051 and the National Science Foundation under Award DMR-0412208.

J. K. Shultis is with the Mechanical and Nuclear Engineering Department, Kansas State University, Manhattan, KS 66506 USA (e-mail: jks@ksu.edu).

D. S. McGregor is with the Mechanical and Nuclear Engineering Department and the Semiconductor Materials and Radiological Technologies (S.M.A.R.T.) Laboratory, Kansas State University, Manhattan, KS 66506 USA (e-mail: mcgregor@ksu.edu).

Digital Object Identifier 10.1109/TNS.2006.872639

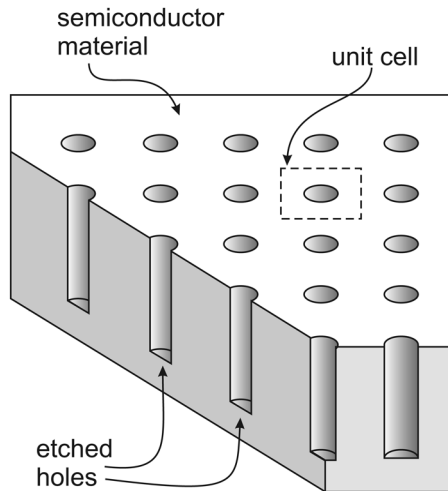


Fig. 1. Conceptual illustration of the basic circular hole design showing a unit cell. The holes shown are subsequently filled with neutron reactive material such as  $^{10}\text{B}$  or  $^6\text{LiF}$ .

as in the present case, and has a macroscopic thermal neutron absorption cross section of  $57.5 \text{ cm}^{-1}$  [12].

### III. DEVICE PERFORMANCE MODELING APPROACH

To increase the detection efficiency of a semiconductor neutron detector, it is proposed that a lattice of holes or cavities be etched into the Si semiconductor material and subsequently filled with  $^{10}\text{B}$  or  $^6\text{LiF}$ . In addition, a film coating of the same neutron reactive material may be applied to the surface through which the perforations are made. However, before building such detectors, it is important to perform design calculations to predict the efficiency of various perforation geometries in order to determine realistic but high-efficiency designs. In this section, a simple calculation model is presented for estimating the detection efficiencies of perforated semiconductor detectors.

#### A. Model Geometry

The designs studied are depicted in Figs. 1 and 2, showing the circular hole design (Fig. 1) and the trench design (Fig. 2). A unit cell, as shown in Fig. 1, consists of a region that is identical to adjacent cells; hence, repeating the unit cell in the  $x$  and  $y$  lateral dimensions produces the basic perforated device. As a result, only a single unit cell need be modeled to provide the expected thermal neutron detection efficiency. Charged particle reaction products exiting the cell at a boundary would be sensed in an adjacent unit cell, hence a reflecting boundary condition for the device is used to include such events. The unit cell for the trench design concept is shown in Fig. 2, in which the cell is repeated in only one dimension ( $x$  direction). The  $y$ -direction is considered infinite in the model since it is the  $x$  and  $z$  directions that determine the effective efficiencies. The main features of a unit cell are shown in Fig. 3, in which there is a defined cell width (and length for the hole design), referred to as the “cell dimension,” a cavity depth, a cavity width (or diameter), and a cap depth, which refers to any extra neutron reactive material covering the entire device above the cavities.

The  $^6\text{Li}(n, t)^4\text{He}$  products have much greater ranges in  $^6\text{LiF}$  ( $6.1 \mu\text{m}$  for the alpha particle and  $32.2 \mu\text{m}$  for the triton) than do

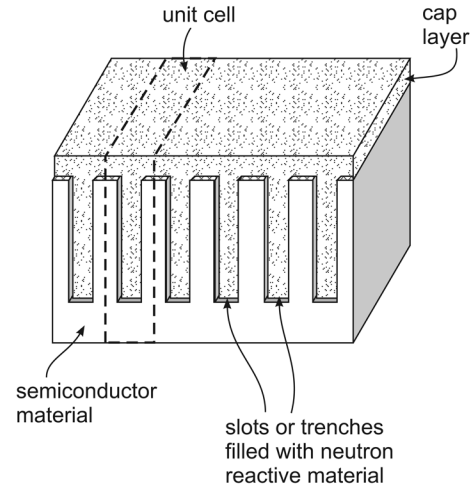


Fig. 2. Conceptual illustration of the basic parallel trench design, showing a unit cell.

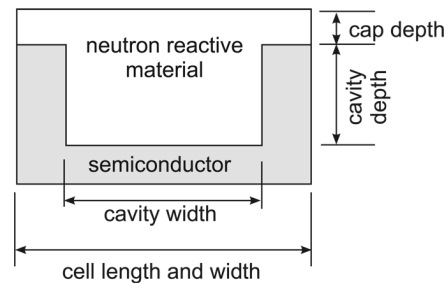


Fig. 3. Cross section of a unit cell, showing the concepts of the perforation depth and width, cell width, and cap thickness.

the  $^{10}\text{B}(n, \alpha)^7\text{Li}$  reaction products in  $^{10}\text{B}$  ( $4.6$  and  $3.7 \mu\text{m}$  for the two alpha particles and  $2.0$  and  $1.8 \mu\text{m}$  for the two Li ions) [12], [19]. Hence,  $^6\text{LiF}$  films can be thicker for coated diode designs than  $^{10}\text{B}$  films [12], and consequently, the perforation and unit cell dimensions can be larger.

#### B. Monte Carlo Simulations of Ion Energy Depositions

In these simulations, a plane parallel beam is assumed to uniformly and normally illuminate the top or bottom of the detector. The silicon semiconductor is assumed transparent to these neutrons and the total cross section for the converter material (LiF or boron) is taken as the ion-producing cross section. Neutron scattering effects are not considered.

By sampling uniformly over the illuminated surface of the detector, a random point  $(x_i, y_i)$  for a neutron incident on the detector surface is determined. Then along a ray through this entry point, a random depth  $z_i$  for a neutron interaction in the converter material is obtained by sampling from the distribution  $f(z) = C \exp(-\Sigma z)$  where  $\Sigma$  is the thermal averaged macroscopic cross section for ion production in the converter material. Here  $C = [1 - \exp(-\Sigma T)]^{-1}$  is a normalization constant to make  $f(z)$  a properly normalized probability distribution function (pdf). The depth  $T$  is the length of the ray through the converter material. If no converter material is in the path of the neutron ray ( $T = 0$ ) then the neutron passes through the detector without interaction. Once a random interaction site  $(x_i, y_i, z_i)$  is determined, a random direction  $\Omega_i =$

$(u_i, v_i, w_i)$ , where  $(u_i, v_i, w_i)$  are the directed cosines for  $\Omega_i$ , for one of the ions is selected from an isotropic directional distribution. The other reaction ion is then given the opposite direction  $(-u_i, -v_i, -w_i)$ . Finally, the identities of the ions are randomly selected according to the branching ratio of the various ions produced in the neutron interaction. The two ions are then tracked along their paths in the detector, and the energy transferred to the silicon regions calculated.

The estimation of the energy deposited in various regions of a silicon semiconductor detector by ions produced by thermal neutron reactions in adjacent regions of boron or lithium fluoride is greatly simplified if all ions are assumed to travel in straight lines, i.e., scattering events and energy straggling can be neglected. Calculation of the energy deposited in the various regions of the detector is then simply a matter of computing the length of the geometric segments an ion travels in each material encountered along its straight-line path from the ion's point of birth to where it is stopped. The energy deposited in the silicon by each simulated ion history is then found by calculating the energy lost by the ion over every path segment it travels through the silicon, as explained in the previous section.

To calculate the energy lost by an ion over each of its path segments, two empirical functions are needed. The first  $E_m^i(x)$  is the mean residual energy after an ion of type  $i$  travels a distance  $x$  in material  $m$ . To obtain this function, the TRIM code [20] was used to obtain a tabulation of the mean residual energy of the various ions produced by thermal neutron interactions in the converter material (LiF or boron) as a function of path length in the converter material and in silicon. Then the Table Curve [21] computer program was used to find an empirical fit to these data. In this way accurate empirical formulas were found for  $E_m^i(x)$  that permitted rapid evaluation of an ion's residual energy. The second function needed for the Monte Carlo calculations is  $X_m^i(E)$ , which is the path length in material  $m$  for the  $i$ th ion to obtain a mean residual energy  $E$ . This function is the inverse of  $E_m^i(x)$ . Again, empirical fits to  $X_m^i(E)$  were also obtained. The function  $X_m^i(E)$  also gives the mean range of the  $i$ th ion in material  $m$ , namely  $R_m^i = X_m^i(0)$ . With these two empirical fits for  $E_m^i(x)$  and  $X_m^i(E)$ , the energy deposited by an ion along any straight-line segment in any of the detector regions can readily be obtained.

Consider an ion that leaves a region composed of material 1 with energy  $E_1$  and enters an adjacent region composed of material 2. The ray in the direction of the ion travel is assumed to have a segment length  $x_2$  in the second region, i.e., the distance from the point where the ion enters the second region to the point where the ray intersects another region, the detector boundary, or is stopped. The problem is to estimate the energy deposited along  $x_2$  and the residual ion energy  $E_2$  (if any) at the end of its path in the second region. Clearly, if the ion with an initial energy  $E_1$  in material 2 has a range less than  $x_2$ , the energy deposited in the second region is  $E_d = E_1$  since  $E_2 = 0$ . However, if this range is greater than  $x_2$ , then  $E_2 > 0$  and the deposited energy is  $E_d = E_1 - E_2$ .

To calculate  $E_2$  at end of the ray in the second medium, we first backtrack the trajectory to find the ion's starting position, were the first medium replaced by the second medium, so as to produce the same residual energy at the interface. This

backtracked distance is  $x_1 = X_1^i(E_1)$ . The energy  $E_2$  after a path length  $x_1 + x_2$ , all in the material of medium 2, is simply  $E_2 = E_2^i(x_1 + x_2)$ . In this manner the energy deposited along any ion track segment can be readily evaluated. The energy the two reaction ions deposit in the silicon regions along their tracks is then recorded in an appropriate bin or tally vector for each simulated reaction event. After performing this simulation for several million reactions, an ideal energy-deposition spectrum is thus obtained.

### C. Simulation of Measured Spectra

The spectrum obtained by the above Monte Carlo procedure is idealized because no energy straggling, large-angle ion scattering or detector noise and resolution effects are considered. A simulated multichannel analyzer (MCA) measured spectrum, which includes such nonideal effects, can be approximated by using a Gaussian averaging or smearing of the counts in each energy bin of the idealized spectrum. The number of counts  $\hat{N}_j$  in the channel  $j$  of the measured spectrum is thus given by [22]

$$\hat{N}_j = \sum_{i=1}^{N_{\max}} N_i W_{ij} \quad (3)$$

where  $N_{\max}$  is the maximum number of MCA energy bins, and  $N_i$  is the number of counts in channel  $i$  of the idealized spectrum. The elements of the *spreading matrix* are

$$\begin{aligned} W_{ij} &= W_{ji} = W_{|i-j|} \\ &= \frac{1}{\sqrt{2\pi}\sigma} \int_{E_j-\Delta}^{E_j+\Delta} \exp\left[-\frac{1}{2}\left(\frac{E_i-E'}{\sigma}\right)^2\right] dE' \\ &= \frac{1}{2} \left\{ \operatorname{erf}\left(\frac{E_j+\Delta-E_i}{\sqrt{2}\sigma}\right) - \operatorname{erf}\left(\frac{E_j-\Delta-E_i}{\sqrt{2}\sigma}\right) \right\}. \end{aligned} \quad (4)$$

Here  $E_i$  is the midpoint energy of MCA energy bin  $i$  with width  $2\Delta$ , and  $\sigma$  is the standard deviation of the smoothing Gaussian. For simulated spectra shown in this report, a standard deviation of  $\sigma = 20$  keV is used. This value has been found to produce spectra typical of those measured for film-coated silicon detectors [22], [23].

### D. Estimation of the Detector Efficiency

The Monte Carlo simulation method described above was used to estimate the overall thermal-neutron detection efficiency, which is defined as the fraction of all thermal neutrons incident on the detector that interact in the converter material and whose subsequent ions deposit at least some minimal amount of energy,  $E_{\text{cut}} = \text{LLD}$ , in the silicon of the detector (300 keV in the present case). In the simulations, a single tally bin was used to record such interactions, thereby allowing the detector efficiency to be estimated without the extra expense of summing the simulated spectra to determine the number of histories depositing energy exceeding  $E_{\text{cut}}$  in the silicon. This number divided by the total number of histories gives the detector efficiency  $\varepsilon$ .

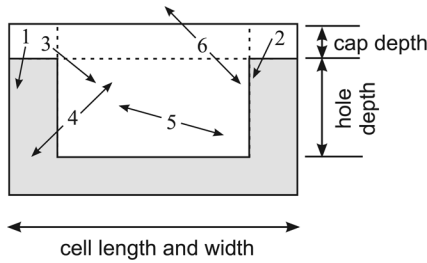


Fig. 4. Six main ion trajectories: 1) interaction occurs in the cap and an ion enters the semiconductor; 2) reaction occurs in the cap and an ion crosses through semiconductor toward reactive material in the cavity; 3) reaction occurs in the cap and an ion enters through the reactive material in the cavity in the direction of the semiconductor; 4) reaction occurs in the cavity below the cap where only the downward reaction ion heads toward the semiconductor; 5) reaction occurs in the cavity below the cap and both ions head toward the semiconductor; and 6) reaction occurs in the cap above the cavity and only the downward ion heads toward the semiconductor.

Closely related to the efficiency of the detector is  $P(n, x)$  defined as the fraction of the incident neutrons that cause an  $(n, x)$  reaction, in which  $x$  represents the lighter of the two product ions. For  $^{10}\text{B}$  and  $^6\text{LiF}$ ,  $\Sigma_c = \Sigma_{(n, x)}$ , so that  $P(n, x)$  also is the fraction of the incident neutrons stopped in the detector or the *stopping fraction*. This quantity, which is usually easy to calculate analytically from the detector geometry, is an upper bound to the detector efficiency, i.e.,  $\varepsilon \leq P(n, x)$ . Moreover, in the limit of very small detectors (compared to the ion ranges), all ions can escape the converter regions and deposit energy greater than  $E_{\text{cut}}$ . Hence, the detector efficiency can be expected to approach  $P(n, x)$  as the detectors become smaller. This limiting case can therefore be used as a verification check for Monte Carlo simulations.

#### IV. RESULTS

##### A. Circular Hole Designs

The circular hole design was analyzed for  $^{10}\text{B}$  and  $^6\text{LiF}$  materials, along with numerous cap layer thicknesses. Here only the optimum results are shown, although a more detailed description of the results can be found elsewhere [19]. Fig. 4 shows the six main trajectories that reaction products can have after neutron absorption in the neutron reactive film. The resulting pulse height spectra for a  $^{10}\text{B}$  filled circular-hole structure is shown in Fig. 5. From this spectrum it is seen that ions born in the rod and that head toward the surrounding silicon (trajectory 5) contribute, by far, the bulk of the deposition spectrum.

The calculated thermal neutron detection efficiencies for the circular-hole design when filled with  $^{10}\text{B}$ , with an additional  $2\text{-}\mu\text{m}$  cap layer, are shown in Fig. 6. The efficiency can be found by selecting a hole diameter and cell dimension, and then dividing the hole diameter by the cell dimension to determine the hole-diameter fraction. The point at which the cell dimension (on the  $x$ -axis) and the hole-diameter fraction (the  $y$ -axis) intersect yields the expected thermal neutron detection efficiency ( $z$  axis). For instance, a cell dimension of  $10\ \mu\text{m}$  with  $6\ \mu\text{m}$  diameter holes has a hole fraction of 0.6, thereby yielding an expected efficiency of 0.16 (or 16%). Hence, 16% of thermal

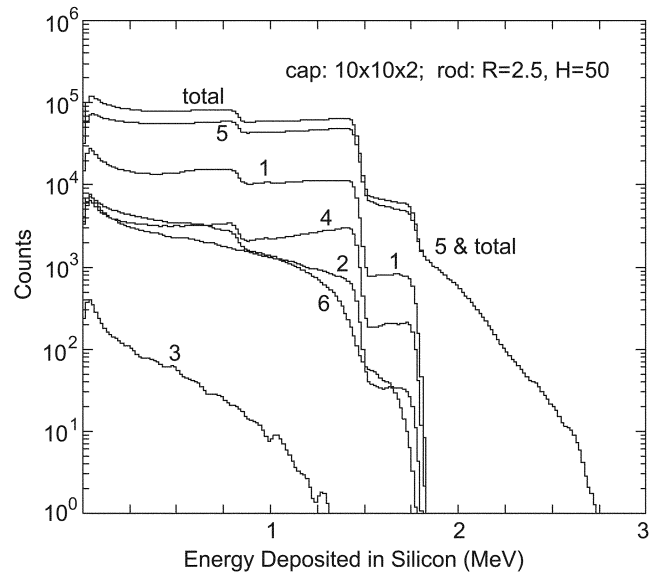


Fig. 5. Energy-deposition spectrum in a  $10 \times 10\ \mu\text{m}$  cell containing a  $50\text{-}\mu\text{m}$  deep  $^{10}\text{B}$ -filled hole  $5\ \mu\text{m}$  in diameter. There is also a  $2\text{-}\mu\text{m}$  cap. Neutrons are normally incident on the cap. Also shown are the contributions from the different ion trajectories shown in Fig. 4.

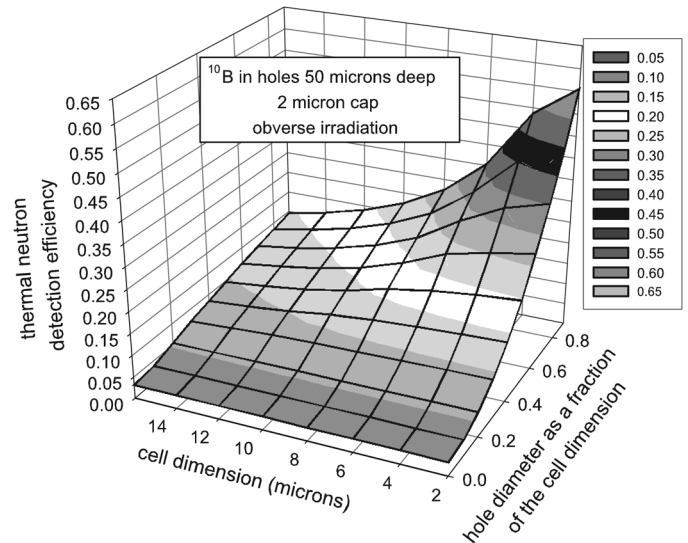


Fig. 6. Calculated thermal neutron detection efficiencies for an obverse irradiated  $^{10}\text{B}$ -filled device with circular holes. The perforations were  $50\ \mu\text{m}$  deep and the device had a  $2\text{-}\mu\text{m}$  thick cap layer.

neutrons crossing the plane of the perforated device will be detected.

Fig. 7 shows the results for obverse irradiation of a  $^6\text{LiF}$  covered device with a  $20\text{-}\mu\text{m}$  cap layer, in which the cell dimensions and cavity fractions are typically larger than  $^{10}\text{B}$  covered devices due to the longer ranges of the  $^6\text{Li}(n, t)^4\text{He}$  reaction products. Using a cell dimension of  $50\ \mu\text{m}$  with a 0.6 cavity fraction ( $30\text{-}\mu\text{m}$  diameter holes), the thermal neutron efficiency is found to be 20.5%. Overall, it is found that  $^6\text{LiF}$ -covered devices yield typically higher efficiencies than  $^{10}\text{B}$ -coated devices.

For a cavity fraction of 0.6, Figs. 8 and 9 show the expected efficiencies for  $^6\text{LiF}$ -covered devices for obverse and reverse irradiation as a function of cap thickness and cell dimension.

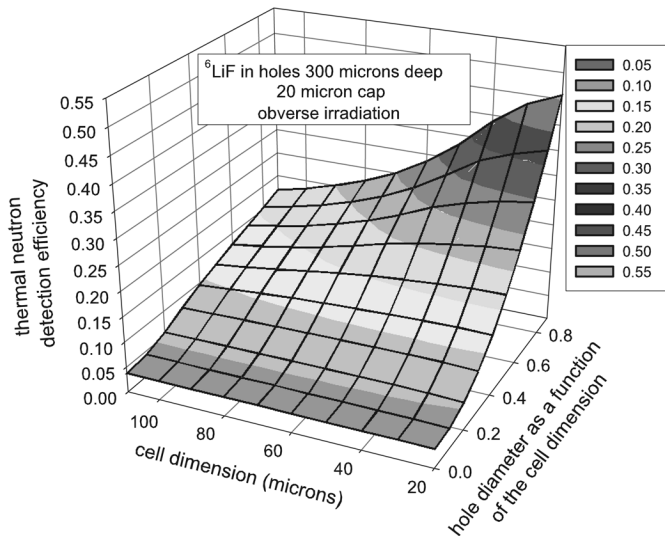


Fig. 7. Calculated thermal neutron detection efficiencies for an obverse irradiated  ${}^6\text{LiF}$ -filled device with circular holes. The perforations were  $300\ \mu\text{m}$  deep and the device had a  $20\text{-}\mu\text{m}$  thick cap layer.

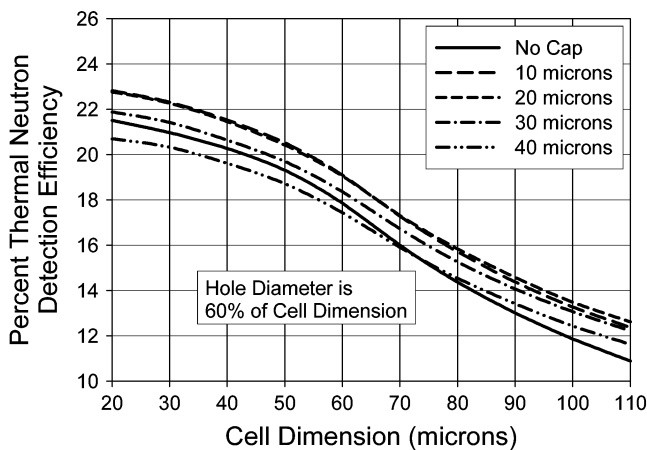


Fig. 8. Efficiencies for various cap layer thicknesses of obverse irradiated  ${}^6\text{LiF}$ -filled circular-hole devices in which the hole diameters were kept at 60% of the cell dimension. The perforations were  $300\ \mu\text{m}$  deep.

It should be noted that (1) efficiencies exceeding 20% can be attained with feature dimensions easily produced with present day dry etching technologies [24], (2) reverse irradiation improves efficiency, and (3) the cap layer thickness must be carefully chosen to optimize performance.

### B. Parallel Trench Designs

An example energy-deposition spectrum for a  ${}^6\text{LiF}$ -filled trench device is shown in Fig. 10 along with the contribution from the various ion trajectories (see Fig. 4). Again, ions produced in the trench dominate the spectrum. The calculated thermal neutron detection efficiencies for reverse irradiation of the parallel-trench design when filled with  ${}^{10}\text{B}$ , with an additional  $2\text{-}\mu\text{m}$  cap layer, are shown in Fig. 11. Similar to previous plots, the efficiency is found by selecting a trench width and cell dimension, and subsequently dividing the trench width by the cell dimension to determine the trench-width fraction. The point at which the cell dimension (on the  $x$ -axis)

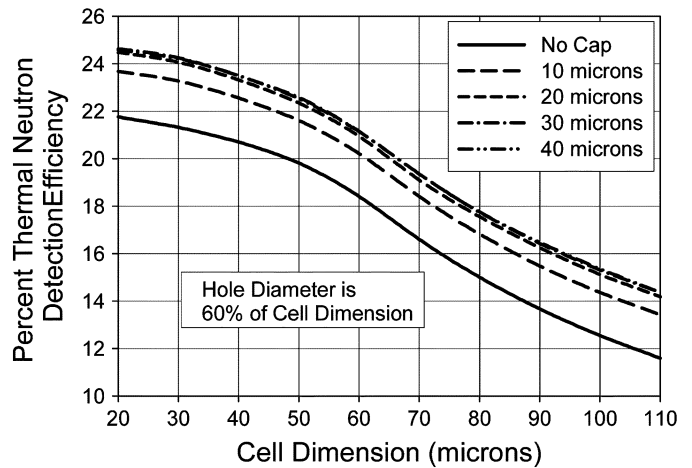


Fig. 9. Efficiencies for various cap layer thicknesses of reverse irradiated  ${}^6\text{LiF}$ -filled circular-hole devices in which the hole diameters were kept at 60% of the cell dimension. The perforations were  $300\ \mu\text{m}$  deep.

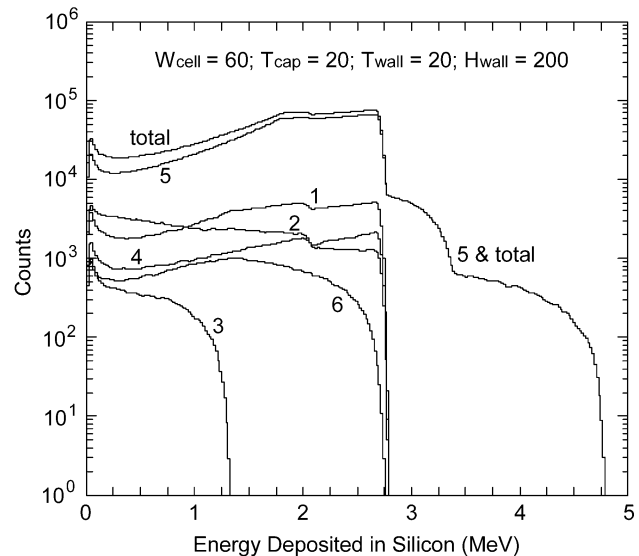


Fig. 10. Estimated energy deposition spectrum for a trench device filled with  ${}^6\text{LiF}$ . Dimensions are in  $\mu\text{m}$ . Also shown are the contributions from the various ion trajectories of Fig. 4.

and the trench width fraction (the  $y$ -axis) intersect yields the expected thermal neutron detection efficiency ( $z$ -axis). Here the trenches and semiconductor fins are kept at the same width. A cell dimension of  $10\ \mu\text{m}$  with  $5\text{-}\mu\text{m}$  wide trenches has a trench fraction of 0.5, thereby yielding an expected efficiency of 0.19 (or 19%). Hence, 19% of thermal neutrons crossing the plane of the trench device will be detected.

Fig. 12 shows the results for reverse irradiation of a  ${}^6\text{LiF}$ -covered device with a  $20\text{-}\mu\text{m}$  cap layer. Using a cell dimension of  $50\ \mu\text{m}$  with a 0.5 cavity fraction ( $25\ \mu\text{m}$  wide), the thermal neutron efficiency is found to be 27%. For a cavity fraction of 0.5, Figs. 13 and 14 show the expected efficiencies for  ${}^6\text{LiF}$ -covered devices for obverse and reverse irradiation as a function of cap thickness and cell dimension. From these results it is seen that 1) efficiencies exceeding 30% can be attained (with dry etching technologies [24]), 2) reverse irradiation improves

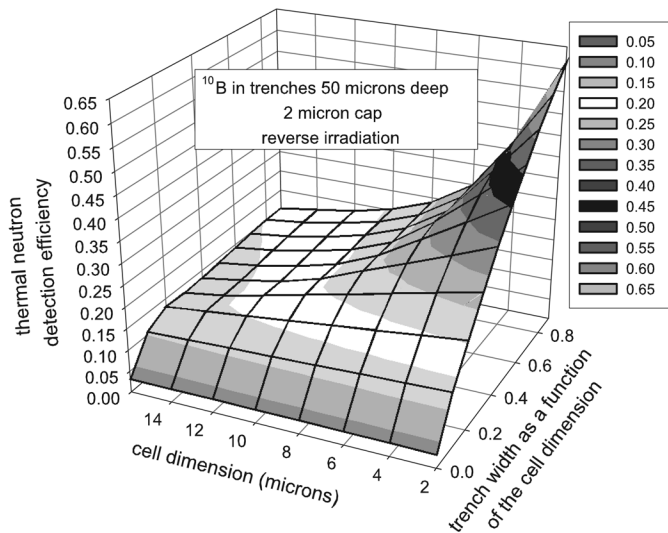


Fig. 11. Calculated thermal neutron detection efficiencies for an obverse irradiated  $^{10}\text{B}$ -filled device with parallel trenches. The perforations were  $50\ \mu\text{m}$  deep and the device had a  $2\text{-}\mu\text{m}$  thick cap layer.

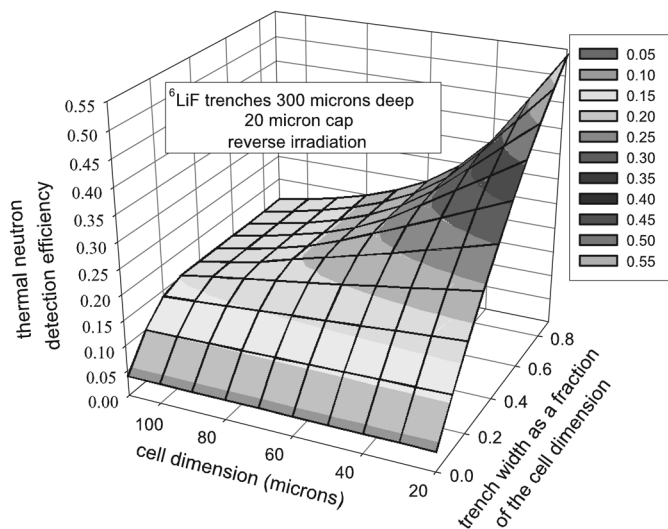


Fig. 12. Calculated thermal neutron detection efficiencies for a reverse irradiated  $^6\text{LiF}$ -filled device with parallel trenches. The perforations were  $300\ \mu\text{m}$  deep and the device had a  $20\text{-}\mu\text{m}$  thick cap layer.

efficiency, and 3) a cap layer thickness of  $20\ \mu\text{m}$  yields near optimum results.

## V. CONCLUSION

Energy deposition calculations indicate that relatively high thermal neutron detection efficiencies can be realized for small cell dimensions with large cavity fractions. However, there is a practical limit on the device dimensions that can actually be fabricated. Hence, reported results are for cell dimensions and cavity fractions that can be easily fabricated with present etching technology, namely, approximately  $10\ \mu\text{m}$  (or more) cell dimensions with 0.5 (or more) cavity fractions. The computed results indicate that the parallel-trench design can provide higher thermal neutron detection efficiencies for similar cell fractions

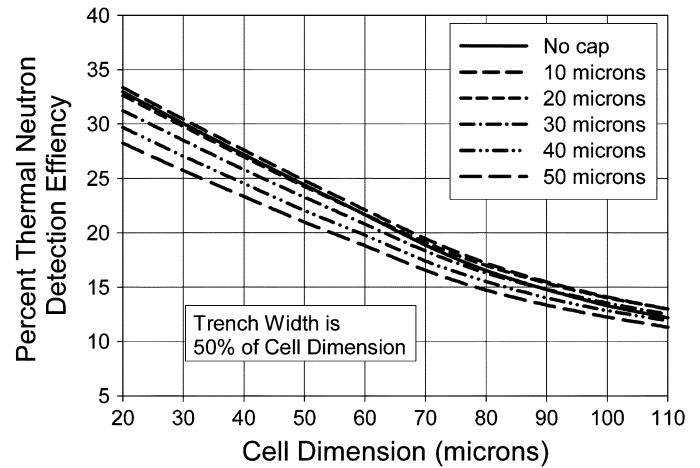


Fig. 13. Efficiencies for various cap layer thicknesses for obverse irradiated  $^{10}\text{B}$ -filled devices with parallel trenches in which the trench widths were kept at 50% of the cell dimension. The perforations were  $300\ \mu\text{m}$  deep.

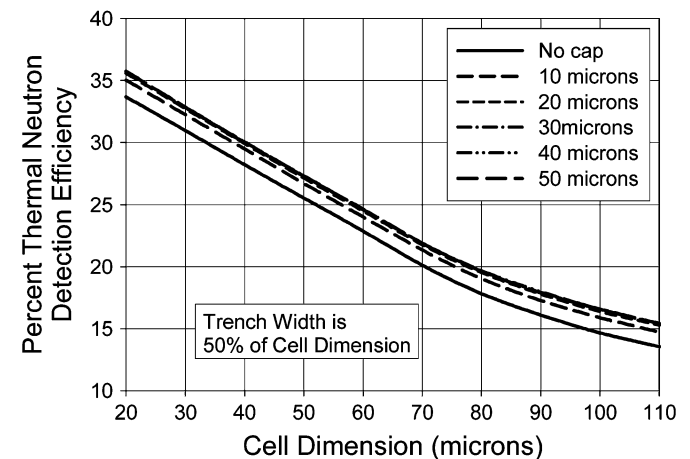


Fig. 14. Efficiencies for various cap layer thicknesses for a reverse irradiated  $^6\text{LiF}$ -filled device with parallel trenches in which the trench widths were kept at 50% of the cell dimension. The perforations were  $300\ \mu\text{m}$  deep.

and dimensions than the circular-hole design. Another observation, discussed elsewhere [19], is that the efficiency increase is predominantly from interaction events occurring in the cavities in which the reaction ion trajectories point toward the cavity walls.

In Figs. 5 and 10, the efficiency for those ions depositing at least  $300\ \text{keV}$  in the semiconductor is noticeably improved by the trajectories described as (5) in Fig. 4, or reactions occurring in the cavity where both reaction product ions head toward the semiconductor. It is also observed, although a small contribution, that the total Q value energy for the reactions described in (1) and (2) can be deposited in the semiconductor detector, a condition not possible for simple thin-film-coated detectors [12].

The increased probability that those reaction products originating in the cavity structures can enter the semiconductor has a pronounced effect upon the attainable thermal neutron detection efficiencies. Hence, the increased efficiency effect is not simply due to increased surface area in contact with the neutron reactive material. From a more practical standpoint, tiny fins of Si on the

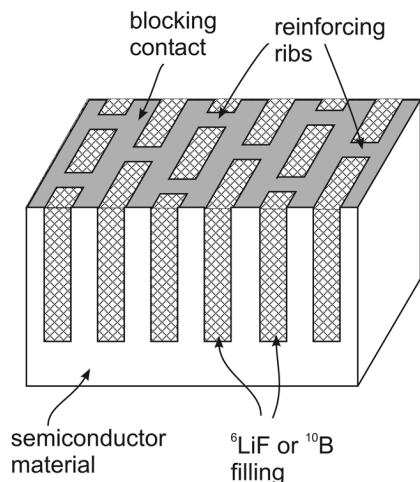


Fig. 15. Modified trench design, composed of parallel trenches with supporting ribs between the semiconductor fins, offers high efficiency and mechanical strength. Two such devices faced inwards in a “sandwich” configuration can yield over 50% thermal neutron detection efficiency.

order of 25  $\mu\text{m}$  or less are quite flexible, and hence can move and bend during the cavity filling process. The circular-hole design would provide a more robust and mechanically sound device despite the fact that it is less efficient than the trench design for neutron detection.

A third option, which is presently the preferred choice of the investigators, is to use the positive aspects of both designs, in which the parallel trench design is strengthened with a matrix of ribs between the semiconductor strips (see Fig. 15). Hence, by folding two such devices together into an inward facing “sandwich” [12], a ribbed trench design capable of 25% thermal neutron detection efficiency can be doubled to produce a compact device capable of 50% thermal neutron detection efficiency.

## REFERENCES

- [1] A. Rose, “Sputtered boron films on silicon surface barrier detectors,” *Nucl. Instrum. Meth.*, vol. 52, pp. 166–170, 1967.
- [2] B. Feigl, H. Rauch, and D. Gd-Neutronenzähler, “Der Gd-Neutronenzähler,” *Nucl. Instrum. Meth.*, vol. 61, pp. 349–356, 1968.
- [3] S. Pospisil, B. Sopko, E. Harrankova, Z. Janout, J. Konicek, I. Macha, and J. Pavlu, “Si diode as a small detector of slow neutrons,” *Radiat. Protection Dosimetry*, vol. 46, pp. 115–118, 1993.
- [4] A. Mireshghi, G. Cho, J. S. Drewery, W. S. Hong, T. Jing, H. Lee, S. N. Kaplan, and V. Perez-Mendez, “High efficiency neutron sensitive amorphous silicon pixel detectors,” *IEEE Trans. Nucl. Sci.*, vol. NS-41, no. 4, pp. 915–921, Aug. 1994.
- [5] D. S. McGregor, J. T. Lindsay, C. C. Brannon, and R. W. Olsen, “Semi-insulating bulk GaAs thermal neutron imaging arrays,” *IEEE Trans. Nucl. Sci.*, vol. 43, no. 3, pp. 1358–1364, Jun. 1996.
- [6] A. R. Dulloo, F. H. Ruddy, and J. G. Seidel, Radiation Response Testing of Silicon Carbide Semiconductor Neutron Detectors for Monitoring Thermal Neutron Flux Westinghouse STC, Pittsburgh, PA, Nov. 18, 1997, Rep. 97-9TK1-NUSIC-R1.
- [7] D. S. McGregor, S. M. Vernon, H. K. Gersch, S. M. Markham, S. J. Wojtczuk, and D. K. Wehe, “Self-biased boron-10 coated high purity epitaxial GaAs thermal neutron detectors,” *IEEE Trans. Nucl. Sci.*, vol. 47, no. 4, pp. 1364–1370, Aug. 2000.
- [8] D. S. McGregor, R. T. Klann, H. K. Gersch, and Y.-H. Yang, “Thin-film-coated bulk GaAs detectors for thermal and fast neutron measurements,” *Nucl. Instrum. Meth. A*, vol. 466, no. 4, pp. 126–141, Aug. 2001.
- [9] H. K. Gersch, D. S. McGregor, and P. A. Simpson, “The effect of incremental gamma-ray doses and incremental neutron fluences upon the performance of self-biased  $^{10}\text{B}$ -coated high-purity epitaxial GaAs thermal neutron detectors,” *Nucl. Instrum. Meth. A*, vol. 489, pp. 85–98, 2002.
- [10] D. S. McGregor, R. T. Klann, H. K. Gersch, E. Ariesanti, J. D. Sanders, and B. VanDerElzen, “New surface morphology for low stress thin-film-coated thermal neutron detectors,” *IEEE Trans. Nucl. Sci.*, vol. 49, no. 4, pp. 1999–2004, Aug. 2002.
- [11] D. S. McGregor, R. T. Klann, J. D. Sanders, J. T. Lindsay, K. J. Linden, H. K. Gersch, P. M. De Lurgio, C. L. Fink, and E. Ariesanti, “Recent results from thin-film-coated semiconductor neutron detectors,” in *Proc. SPIE*, 2002, vol. 4784, pp. 164–182.
- [12] D. S. McGregor, M. D. Hammig, H. K. Gersch, Y.-H. Yang, and R. T. Klann, “Design considerations for thin film coated semiconductor thermal neutron detectors, part I: Basics regarding alpha particle emitting neutron reactive films,” *Nucl. Instrum. Meth. A*, vol. 500, pp. 272–308, 2003.
- [13] C. Petrillo, F. Sacchetti, O. Toket, and N. J. Rhodes, “Solid state neutron detectors,” *Nucl. Instrum. Meth. A*, vol. 378, pp. 541–551, 1996.
- [14] A. J. Peurrung, “Recent developments in neutron detection,” *Nucl. Instrum. Meth. A*, vol. 443, pp. 400–415, 2000.
- [15] V. McLane, C. L. Dunford, and P. F. Rose, *Neutron Cross Sections*. San Diego, CA: Academic, 1988, vol. 2.
- [16] D. S. McGregor and R. T. Klann, “Pocked Surface Neutron Detector,” U.S. Patent 6 545 281, Apr. 8, 2003, allowed.
- [17] G. F. Knoll, *Radiat. Detection and Measurement*, 3rd ed. New York: Wiley, 2000.
- [18] D. I. Garber and R. R. Kinsey, *BNL 325: Neutron Cross Sections*, 3rd ed. Upton, NY: Brookhaven Nat.Lab., 1976, vol. 2, Curves.
- [19] J. K. Shultis and D. S. McGregor, Calculation of Ion Energy-Deposition Spectra in Silicon, Lithium-Fluoride, Boron, and Boron Carbide Engineering Experiment Station, Kansas State University, Manhattan, KS, 2004 [Online]. Available: <http://ww2.mne.ksu.edu/~jks/papers/EESrpt299.pdf>, referenced on Sep. 20, 2005
- [20] J. F. Ziegler and J. P. Biersack, *Transport of Ions in Matter in SRIM-2003 Code, Version 26*. : IBM Corp., 2003 [Online]. Available: <http://www.srim.org>
- [21] *TableCurve*. San Mataso, CA: Jandel Scientific, 1996.
- [22] D. S. McGregor and J. K. Shultis, “Spectral identification of thin-film-coated and solid-form semiconductor neutron detector,” *Nucl. Instrum. Meth. A*, vol. 517, pp. 180–188, 2004.
- [23] ———, “Response to the ‘comment’ by S. Hallbeck,” *Nucl. Instrum. Meth. A*, vol. 536, pp. 232–234, 2005.
- [24] *Process Performance Notes for PlasmaLab System 100*. : Oxford Instruments, SI2-2P.1.